Supplementary Information

S1. SAMPLE & EXPERIMENTAL SETUP

The sample used is a $5\lambda/2$ AlGaAs/GaAs microcavity, composed by 32 (35) top (bottom) distributed Bragg reflectors (DBRs) and 4 triplets of 10 nm thick GaAs QWs. The cavity quality factor is measured to exceed $Q \gtrsim 8000$, with transfer matrix simulations giving $Q = 20000$, corresponding to a cavity photon lifetime ~ 9 ps. The Rabi splitting is 9 meV. This is the the same sample used in Ref. [1]. All the data presented here are recorded at negative detuning $\Delta = -4$ meV.

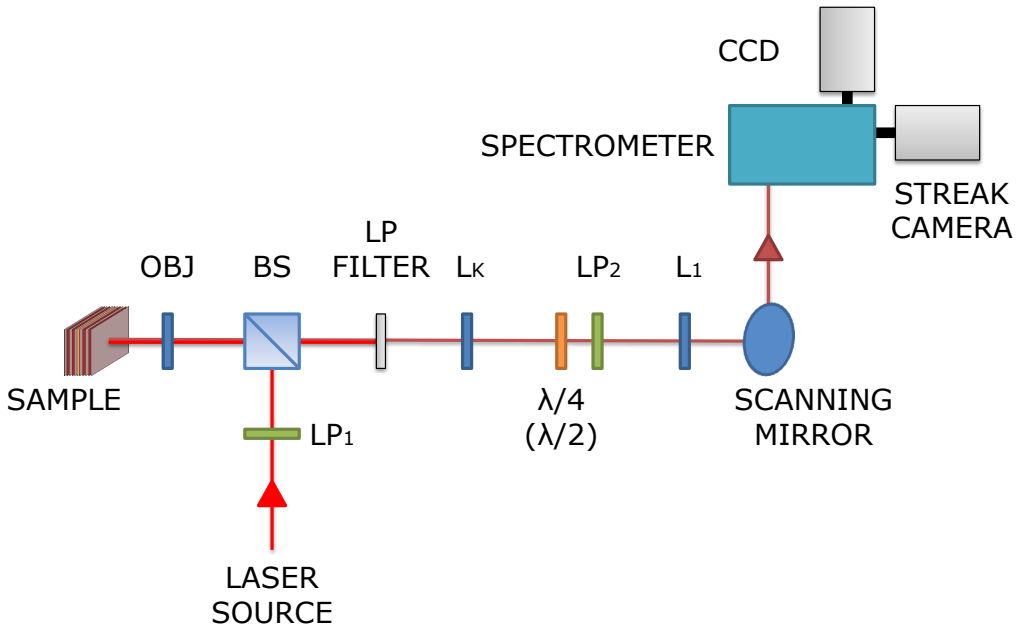

Figure **S1**. Sketch of the experimental setup. Lists of the optical components: $\mathbf{LP}_1$ is the linear polarizer with extinction ratio higher than 1000:1; **BS** is the non-polarizing beam splitter; **OBJ** is the 20x, 0.4 NA objective; **LP Filter** is the long pass filter; $\mathbf{L}_k$ is the lens used to imagine the k-space; $\lambda/4$ ($\lambda/2$) is the quarter-wave plate (half-wave plate); $\mathbf{LP}_2$ is a linear polarizer and **L1** is the 10 cm focal length lens. The motorized scanning mirror and the spectrometer, equipped with both a charge coupled device (CCD) and a streak camera, are also shown.

The dynamic of polaritons is studied by using the experimental setup shown in Fig. S1. We use a pulsed laser, with pulse width of 250 fs and a pulse frequency of 80 MHz. The sample is held in a helium cryostat at temperature $T = 6$ K and all the experiments are performed under non-resonant excitation. The excitation laser, tuned to the first spectral minimum above the high-reflectivity mirror stopband at 1.653 eV, is focused to a spot of ~ 2 μm FWHM ($2\sqrt{\ln(2)}\sigma$) (with σ being the standard deviation of the 1D Gaussian curve used to fit the spot intensity profile), by means of a 0.4 numerical aperture objective. The power of the excitation is at 7 mW. The excitation beam is linearly polarised with polarization extinction ratio higher than $1{:}10^3$.The polarized emission is collected by the same objective, sent through a long pass filter (to filter out the laser), analyzed by a polarimeter composed of a $\lambda/2$ or $\lambda/4$ plate and a linear polarizer (LP_2) and then projected with an achromatic lens L_1 (f = 10 cm) on the entrance slit of a spectrometer. The latter is equipped with both a charge coupled device (CCD) and a streak camera with 2 ps temporal resolution. The grating of the spectrometer can be interchanged with a mirror allowing direct imaging of real or momentum (k) space without energy resolution. To measure the far field emission of the microcavity, i.e., the k-space, an extra lens L_k (f = 30 cm) is used to form the image of the Fourier plane onto the entrance slit of the spectrometer.

In order to study the polarization dynamics in both real and k-space, without energy resolution, the intensity emitted by the microcavity is time-resolved by using a tomography scanning technique. In this technique, the near field intensity I(t,x,y) [far field I(t,k_x,k_y)] emitted by the microcavity is imaged on the entrance slit of the streak camera for a fixed y [k_y]. By using a motorized mirror, it is possible to scan the y [k_y] dimension and acquire I(t,x)

[I(t,k_x)] at different y [k_y]. In this way, a 2D real space image I(x,y) [2D k-space image I(k_x,k_y)] at different times can be reconstructed. In the case of k-space this is possible since photons, emitted from the microcavity at an angle θ (where θ is the emission angle with respect to the normal of the microcavity plane), correspond to polaritons with in-plane wavevector $k_{||} = k_0 \sin(\theta)$ (with $k_0 = 2\pi/\lambda_0$ and λ_0 being the emission wavelength). The data reconstruct with this technique are Fig.1 (a-c) of the manuscript, Fig.**S6** (a-c) and the videos (S1-S3) for the 2D real space and the video S4 for the k-space. In order to take into account the different delay introduced by the waveplates, when the different polarization components are measured, the experimental data have been rescaled to have a common zero, where zero time is defined at the photoluminescence onset. This correction has been applied to both the Stokes images and the intensity profiles presented in this work.
Finally, the tomography scanning technique has been also used to perform energy resolved measurements of the spin texture [Fig.4 (a-b) of the manuscript]. In this case the emission from the microcavity is focused on the entrance slit of the spectrometer with the grating now active (for the spectral selection of the ultrashort pulses) and then projected on the CCD. The motorized mirror allow to scan the wavelength (λ) on the grating and acquire I(x,y) at different λ. Successively, a 2D real space image I(x,y) at different λ can be reconstructed.

S2. SPIN WHIRLS IN PRESENCE OF DISORDERS

In Fig.**S2**(a-c), the formation of polariton spin whirls is calculated in presence of disorders, resembling the experimental results shown in Figs.1(a-c) of the main manuscript. The parameters used to perform the simulations are the same used for Figs.1(a-c) of the main manuscript [2]. The disorder potential was generated with 0.05 meV root mean squared amplitude and 1.5 μm correlation length. The theoretical calculations show that, although disorder introduces some additional fine structure, it does not affect the basic spin textures.

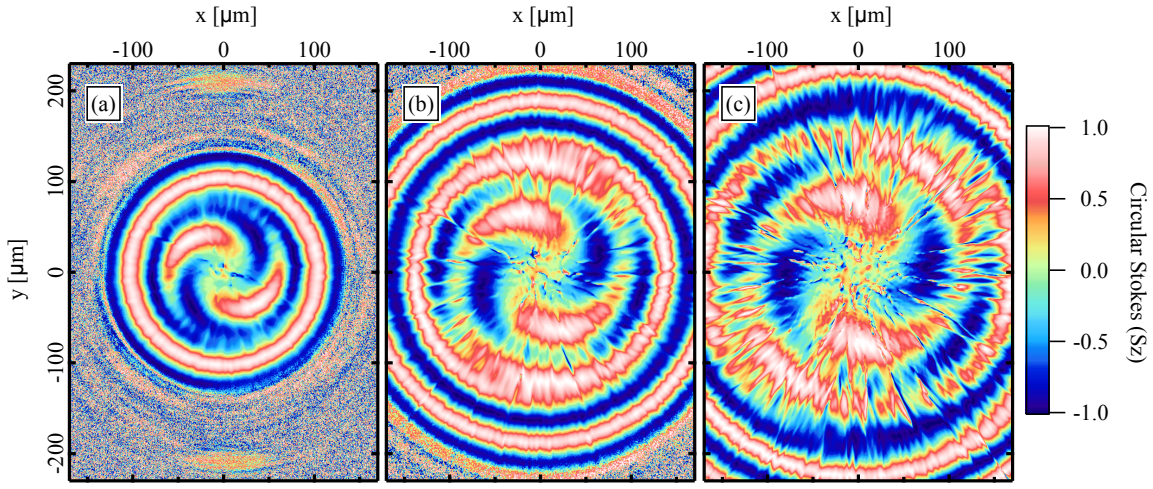

Figure **S2**. (a-c) Theoretical simulations showing the circular Stokes vector S_z of the spin whirls in presence of disorders at (a) 30 ps, (b) 45 ps and (c) 60 ps. The parameters used in the simulations, reported in Ref.[2], are the same as Fig.1(d-f) of the main manuscript.

S3. ELLIPTICITY OF THE EXCITATION SPOT

As has been shown by Richards and Wolf [3], the tight focusing of a polarized Gaussian beam through a high numerical aperture (NA) lens, results in the modification of the polarization at focal plane. In particular, the electric field of a linearly polarized beam, when focused by a high NA objective, acquires non-zero components in the two directions perpendicular to the polarization of the incident field (i.e., at the focus plane the electric field vector sweeps an ellipse) [3–6]. For a review see Ref. [7]. In our experiments, the polarization at the pump spot has been measured by focusing a linearly polarized beam with a 0.4 NA objective (the same used in the experiment) on a glass. The transmitted intensity has been collected with a 100x, 0.7 NA objective. In order to measure the polarization of the beam, we used a polarimeter composed of a $\lambda/2$ or $\lambda/4$ plate and a linear polarizer. The emission is then imaged in real space by a 20 cm focus lens directly on a CCD camera. The linear (S_x), diagonal (S_y) and circular (S_z) Stokes

parameters measured are reported respectively in Figs. **S3** (a-c).

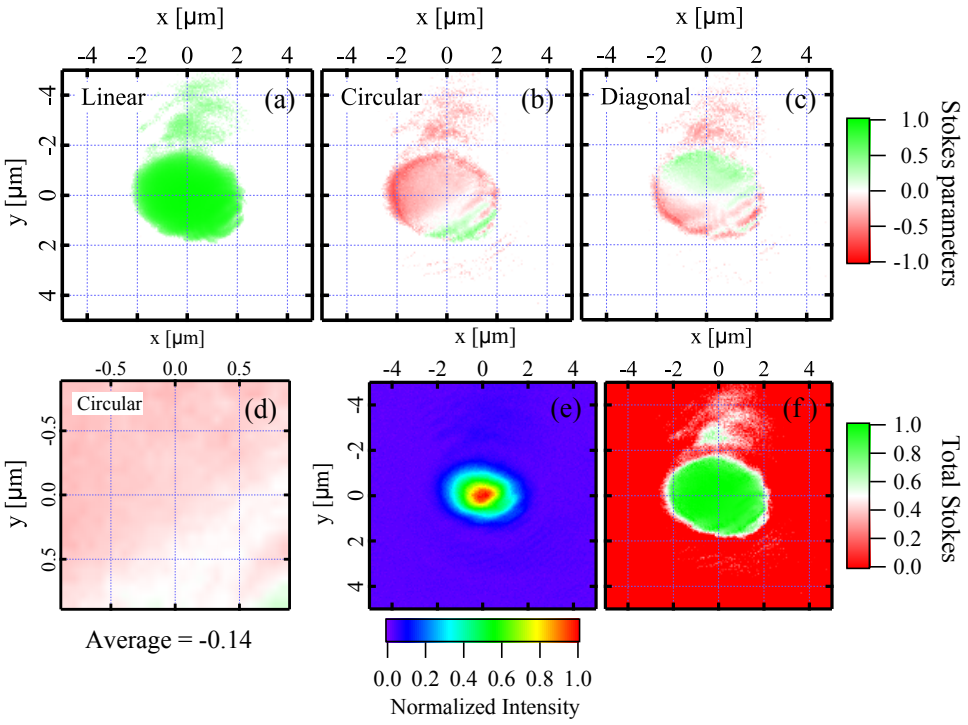

Figure **S3**. (a) Linear, (b) circular and (c) diagonal Stokes parameters of the beam spot focused by a 0.4 numerical aperture objective. (d) Zoom of the circular component reported in (b) on an area of $(1.78\,\mathrm{x}1.78\,)\mu m^2$ comparable with the area of the 2 μm FWHM excitation spot used in the experiment. The average of the circular Stoke components is -0.14. (e) Real space intensity of the circularly polarized pump spot (σ_-). (f) Total degree of polarization S_{tot} calculated from (a), (b) and (c).

The Stoke parameters $\mathrm{S}_{x,y,z} = (I_{H,D,\Psi_+} - I_{V,A,\Psi_-})/I_{tot}$, with I_{H,D,Ψ_+} and I_{V,A,Ψ_-} being the measured intensity in the horizontal (H), vertical (V), diagonal (D), antidiagonal (A) and the two circular (Ψ_+, Ψ_-) polarization components. $I_{tot} = I_{H,D,\Psi_+} + I_{V,A,\Psi_-}$ is the total emission. We estimate the circular value of ellipticity by averaging the circular Stokes parameters over an area of $(1.78\,\mathrm{x}1.78\,)\mu m^2$ comparable with the area of the 2 μm FWHM excitation spot used in the experiment, as shown in Fig.**S3** d). The average value of the circular stokes parameters is -0.14 justifying the 10% ellipticity used in the theoretical simulations. In Fig.**S3** e) and Fig.**S3** f) the intensity of the beam in real space for the circular component (σ_-) and the total degree of polarization calculated as $\mathrm{S}_{tot} = \sqrt{S_x^2 + S_y^2 + S_z^2}$ are also reported for the sake of completeness.

S4. POLARITON AND EXCITON RESERVOIR DYNAMICS

In Fig.**S4**, the intensity of the polarization components integrated over space is plotted versus time in the case of linearly polarized pump and circular detection [Fig.**S4** (a)] and circularly polarized pump and linearly detection [Fig.**S4** (b)], corresponding respectively to the intensity profiles of Fig.1 of the main manuscript and Fig.**S6** of the supplementary information (see Sec.S5). In both cases the area of integration is $(460\,\mathrm{x}\,340\,)\mu m^2$. To take into account the different delays introduced by the waveplates, the intensity profiles have been scaled in order to have a common zero. In the case of linearly polarized pump [Fig.**S4** (a)] the small imbalance between Ψ_+ and Ψ_- introduced by the high-NA objective, results in picosecond scale oscillation in the circularly polarized emission (similarly to the one observed in Ref. [8]), which coincides with the rotation of the spin textures.
Therefore, by referring to Fig. **S4** (a), we can identify three different regimes in the formation dynamics of the spin whirl. Up to 38 ps, the dynamics of the polariton is mainly characterized by the propagation of polaritons radially out of the excitation spot (see the supplementary video S2) which corresponds to the formation of a 2D spin texture in the plane of the microcavity. Once the 2D spin textures are formed, corresponding to the point of maximum intensity of Ψ_+ and Ψ_- polaritons, they start to rotate. This regime, indicated in Fig. **S4** (a) as "Rotation regime", corresponds to the appearance of the spin whirl [Figs. 1 (a-c) of the main manuscript] and the inversion of the polarization at the

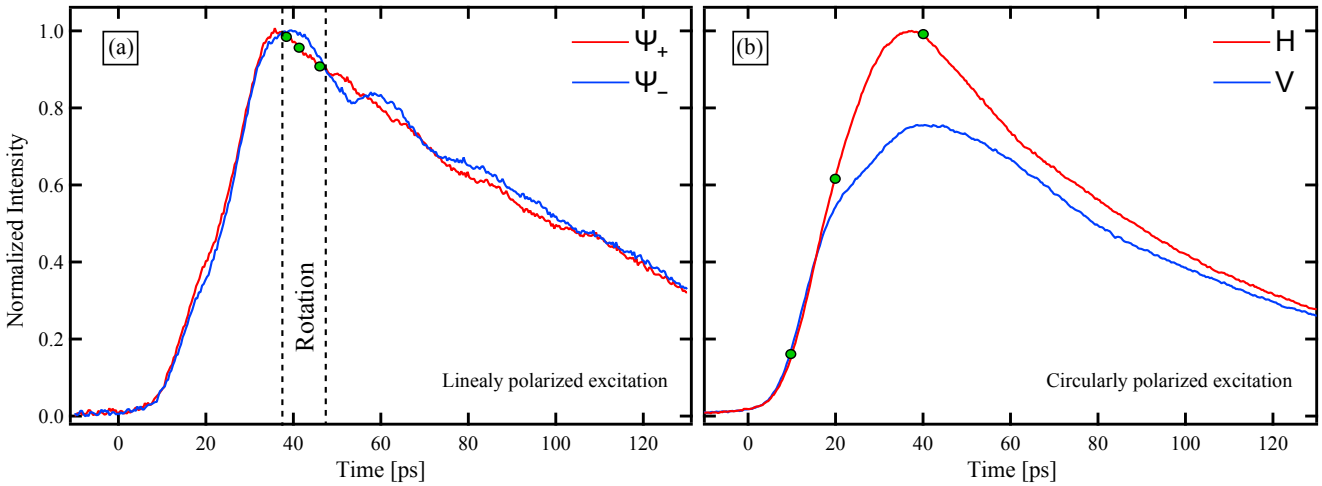

Figure **S4**. Time-resolved, spatially integrated measurements under (a) linearly polarized excitation and circular detection and (b) circularly polarized excitation and linear detection. In both cases the intensity profiles versus time have been integrated over an area $(460\,\mathrm{x}340\,)\mu m^2$ corresponding to the one imaged in Fig.1 of the manuscript and Fig.**S6** of the supplementary information. The solid green circles in (a) and (b) correspond respectively to the time where the snapshots in Fig.1 (a-c) of the manuscript and Fig.**S6** (a-c) of the supplementary information have been extracted.

pump spot position [Fig. 3(a) of the main manuscript]. In the case of circularly polarized excitation, on the other hand, the imbalance between the two polariton populations set by the pump will be preserved throughout the entire process and no oscillations in the density appear [Fig. **S4** (b)].

In Fig.**S5** the dynamics of the polariton condensate and exciton reservoir [Fig.**S5** (a)], under elliptically polarized pump, is studied and compared with the energy splitting [Fig.**S5** (b)] and the polarization at the pump spot position [Fig.**S5** (c)]. Starting from a linearly polarized condensate shown in Fig.**S5** (a), the evolution of the polarization follows hand in hand with the splitting [Fig.**S5** (b)]. Specifically, one should note the sudden change in the polarization behavior as the splitting reverses (grey dashed line), corresponding to the Stokes vector reversing its precession in Fig.**S5** (c). The rotational direction is controlled by the sign of the splitting. Positive splitting induces anti-clockwise rotation while negative splitting a clockwise one. When Ψ_+ polaritons are generated faster they deplete the $\mathcal{N}_+$ excitons, causing the density to suddenly drop faster than $\mathcal{N}_-$ and thus changing the sign of the splitting. Numerically, the spin +1 polaritons condense first since they are being pumped at a higher rate due to the ellipticity of the pump. This is displayed as a concentric polarization ring which expands outward. Then, as $S_z = -1$ polaritons condense and the reservoir densities deplete (i.e. the splitting switches from weak positive to strong negative) the spin whirl appears.

A notable difference exists between the experiment and the simulation. Experimentally, as noted earlier, there is an equal and steady formation of the spin components (under elliptical pumping) which at their maximum intensity suddenly rotate [Fig. **S4** (a)]. From the GPE model [Eqs. (1) and (2), main manuscript] the imbalance set by the pump immediately causes an imbalance in the exciton reservoir components, $\mathcal{N}_\pm$. When the polaritons condense, the $\Psi_\pm$ populations grow at different rates [blue and red line in Fig.**S5** (a) unlike the steady growth seen in Fig.**S4** (a)] leading up to the whirl. This causes an immediate appearance of the spin whirl in the simulations from the moment of condensation and splitting reversal (Fig.**S5**, gray dashed line). Qualitatively the rotation observed in experiment is the same as depicted by the GPE model. To achieve more accurate dynamics, a multiple-reservoir model would be more suitable.

Single Reservoir Model. Typically polariton condensation is described with the use of a single reservoir model [9]. This approach is known to result in an exaggerated depletion of the reservoir, which is emptied once condensation is stimulated. Accurate descriptions of polariton condensate dynamics require the multi-level structure of the reservoir to be accounted for [10, 11]. However, the single reservoir model is able to predict the spatial pattern of the spin whirl, which is the main focus of our work, and its qualitative rotation in time. To avoid using an overly complicated model to describe this effect, we prefer the single reservoir model, while sacrificing an exact match to the timescales observed experimentally (in Fig.**S5**).

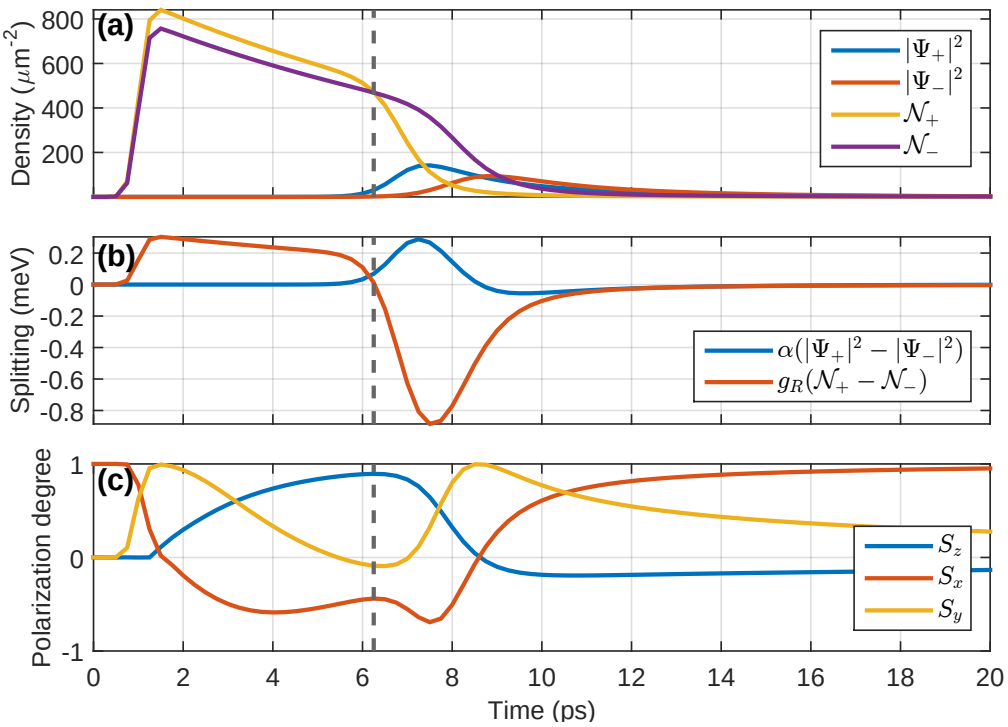

Figure **S5**. Dynamics of the condensate and reservoir at the pump position under elliptical pumping extracted from the simulation in Fig.2 (c) of the main manuscript. (a) Density versus time of the $\Psi_\pm$ polariton condensate and $\mathcal{N}_\pm$ exciton reservoir. (b) Energy splitting versus time of the polariton condensate (blue line) and exciton reservoir (orange line). (c) Linear (S_x), diagonal (S_y) and circular (S_z) Stokes components versus time, extracted at the pump spot position. The dashed grey line indicates the position where the energy splitting in (b) and the Stoke vector in (c) reverse.

S5. CIRCULARLY POLARIZED EXCITATION

As mentioned in the main manuscript, we have repeated the same experiments at the same conditions of detuning (-4 meV), power (7 mW) and excitation spot (2 μm FWHM) but now exciting with a circularly polarized beam. The experimental results are shown in Fig.**S6** and in the supplementary video S3. In the case of circularly polarized excitation shown in Fig. **S6**, polariton condensation results in highly imbalanced population [Fig. **S4** (b)] and the small ellipticity induced by the tightly focused spot will not play a relevant role as in the case of linearly polarized pump. As a consequence, the imbalance between the two polariton populations is set by the pump and preserved throughout the entire process, so that the polarization do not rotate at the pump spot. Therefore, no oscillation in the density [Fig. **S4** (b)] and in the polarization at the pump spot [Fig.**S6** (d)] appear and the orientation of the four-leaf clover pattern typical of the OSHE, remain fixed in time (i.e the spin texture does not rotate). As polaritons propagate radially outward in the plane of the microcavity, their spin precesses around Ω_{LT}, giving rise to characteristic shape domains already observed in Ref. [1].

In the simulations shown in Fig. **S7**, we use a nearly circular pulse, where the ellipticity is set to $\sigma_+ = 1$, $\sigma_- = 0.1$. The other parameters were set to: $\alpha = 2.4$ μeV μm^2, $g_R = 1.5\alpha$, $G = 4\alpha$, $r_c = 0.01$ μm^2 ps^{-1}, $\Delta_{LT}/k_{LT}^2 = 11.9$ μeV μm^2, $\tau_p = 9$ ps, $\tau_x = 10$ ps.

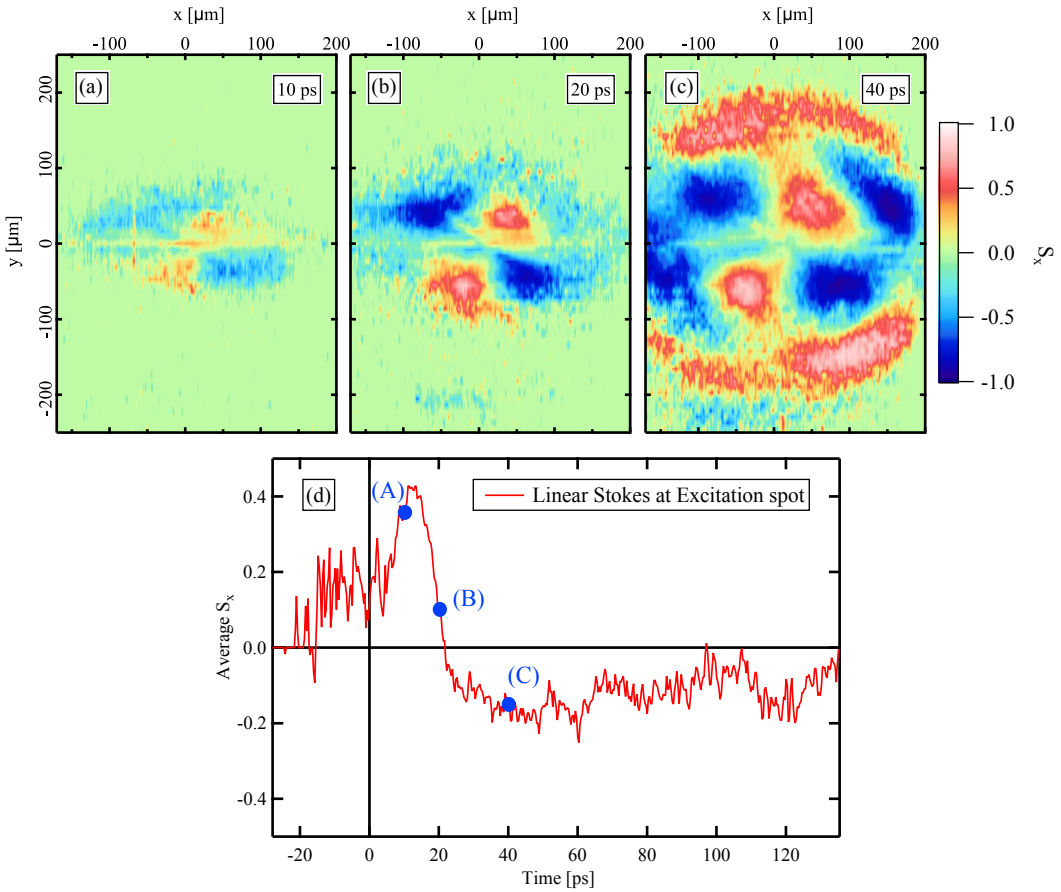

Figure **S6**. Real space experimental Stokes parameters at (a) 10 ps, (b) 20 ps and (c) 40 ps showing the evolution in time of the linear component within the microcavity plane. The excitation beam is circularly polarized and at 1.653 eV energy. After the hot excitons relax down on the lower polariton dispersion, polaritons are formed with $k \leq 2.8\,\mu m^{-1}$. See supplementary video S3 for the full dynamics in real space. (d) Linear degree of polarization versus time calculated by averaging the experimental circular Stokes parameters over an area of $(1.78\,x1.78\,)\mu m^2$, centered around $(0,0\,)\mu m$ in Figs. (a-c), comparable with the area of the 2 μm FWHM excitation spot used in the experiment. The letters (A), (B) and (C) in the graph refer to Figs. (a-c)

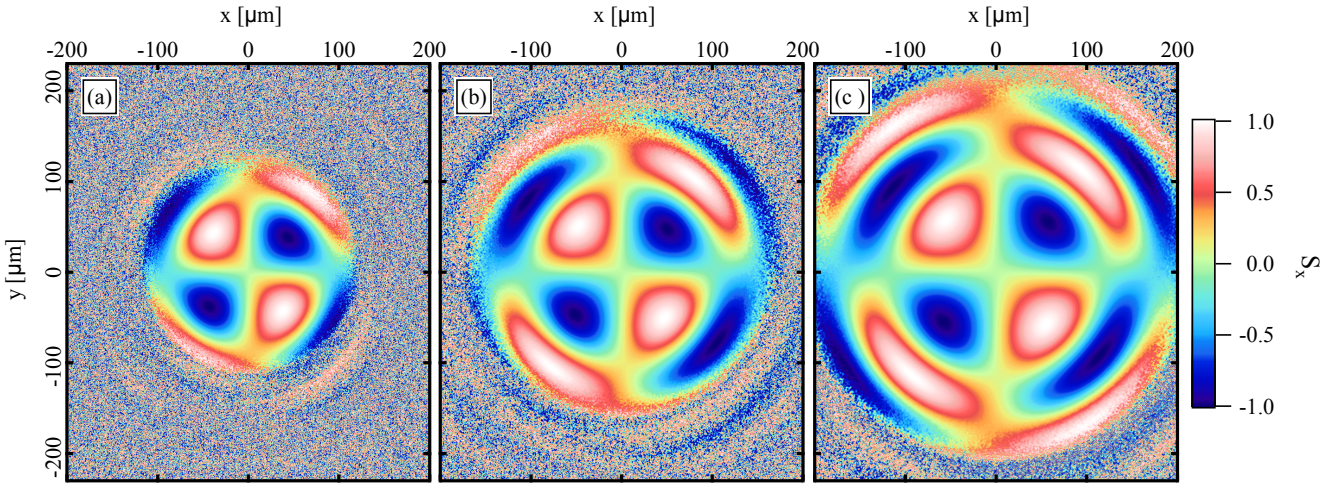

Figure **S7**. Theoretical linear Stokes parameters at (a) 40 ps, (b) 55 ps and (c) 70 ps showing the formation and evolution of the linear Stokes spin texture in the plane of the microcavity. The polarization of the excitation beam is set to $\sigma_+ = 1$, $\sigma_- = 0.1$.

[1] E. Kammann, T. C. H. Liew, H. Ohadi, P. Cilibrizzi, P. Tsotsis, Z. Hatzopoulos, P. G. Savvidis, A. V. Kavokin, and P. G. Lagoudakis, Phys. Rev. Lett. **109**, 036404 (2012).

[2] *In all the theoretical calculations the following parameters were set to:* $\alpha = 2.4\ \mu eV\ \mu m^2$, $g_R = 1.5\alpha$, $G = 4\alpha$, $r_c = 0.01\ \mu m^2\ ps^{-1}$, $\Delta_{LT}/k_{LT}^2 = 11.9\ \mu eV\ \mu m^2$, $\tau_p = 9\ ps$, $\tau_x = 10\ ps$.

[3] B. Richards and E. Wolf, Proceedings of the Royal Society of London A: Mathematical, Physical and Engineering Sciences **253**, 358 (1959).

[4] J. Lekner, J. Opt. A: Pure Appl. Opt. **5**, 6 (2003).

[5] R. Dorn, S. Quabis, and G. Leuchs, Journal of Modern Optics **50**, 1917 (2003).

[6] H. Kang, B. Jia, and M. Gu, Opt. Express **18**, 10813 (2010).

[7] Z. Chen, L. Hua, and J. Pu, in *Progress in Optics*, Progress in Optics, Vol. 57, edited by E. Wolf (Elsevier, 2012) pp. 219–260.

[8] M. D. Martin, G. Aichmayr, L. Viña, and R. André, Phys. Rev. Lett. **89**, 077402 (2002).

[9] M. Wouters, I. Carusotto, and C. Ciuti, Phys. Rev. B **77**, 115340 (2008).

[10] K. G. Lagoudakis, F. Manni, B. Pietka, M. Wouters, T. C. H. Liew, V. Savona, A. V. Kavokin, R. André, and B. Deveaud-Plédran, Phys. Rev. Lett. **106**, 115301 (2011).

[11] C. Anton, T. C. H. Liew, G. Tosi, M. D. Martin, T. Gao, Z. Hatzopoulos, P. S. Eldridge, P. G. Savvidis, and L. Vina, Phys. Rev. B **88**, 035313 (2013).